Tribology International 140 (2019) 105893

Contents lists available at ScienceDirect

Tribology International

journal homepage: www.elsevier.com/locate/triboint

Measurement of strain evolution in overloaded roller bearings using energy dispersive X-ray diffraction

A. Reid[a,*], C. Simpson[b], I. Martinez[a], S. Kabra[c], T. Connolley[d], O. Magdysyuk[d], C. Charlesworth[d], M. Marshall[a], M. Mostafavi[b]

[a] University of Sheffield, Dept. Mechanical Engineering, Sheffield, S1 3JD, UK
[b] University of Bristol, Dept. Mechanical Engineering, Bristol, BS8 1TR, UK
[c] STFC-Rutherford Appleton Laboratory, ISIS Facility, Harwell, OX11 0QX, UK
[d] Diamond Light Source Ltd, Harwell Science and Innovation Campus, Didcot, Oxfordshire, OX11 0DE, UK

ARTICLE INFO

Keywords:
Energy dispersive X-ray diffraction
Stroboscopic strain
Rolling contact fatigue
Bearing overload

ABSTRACT

There are several mechanisms contributing towards detrimental damage in wind turbine gearbox bearings, with sudden overload events believed to reduce their expected operational life. The generation of subsurface plasticity, followed by rolling contact fatigue, may lead to the initiation of either surface or subsurface cracking. This study presents a novel technique capable of measuring subsurface strain evolution in a rotating roller bearing, using energy dispersive X-ray diffraction. A pre-overloaded bearing was tested dynamically and consequently failed prematurely, supporting the hypothesis that overloads accelerate bearing failure. Throughout the test, an increase in compressive radial strain was observed, indicative of material softening, generally associated with the unstable stage of rolling contact fatigue, which occurs prior to definitive bearing failure.

1. Introduction

1.1. Background

Premature failure of wind turbine gearbox (WTG) bearings is an area of great importance for industry due to significant interruptions to regular operating conditions [1]. The downtime for a single WTG failure is generally reported to be longer than for other constituent systems, with bearing failure suspending regular operation for up to 562 h [2,3]. Damage reports completed by the National Renewable Energy Laboratory in USA found that as much as 70% of gearbox component failure was related to bearings [4]. Research and development of condition monitoring systems, such as acoustic emission measurement and vibration analysis, is currently crucial for saving time and money for wind turbine operators, as these techniques may offer the opportunity to identify a faulty bearing prior to a failure [5]. The cause of WTG bearing failures has conventionally been diagnosed post mortem, with in situ techniques now becoming important for real-time validation.

The drivetrain of a wind turbine conventionally consists of several large cylindrical or tapered roller bearings, capable of withstanding the substantial loads exerted during normal operation. One of the most prominent locations for failure is at a bearing that supports the high-speed shaft (HSS), operating with rotational frequencies of up to 1800 revolutions per minute (*rpm*) [6,7]. Even when installed and maintained carefully, it is established that bearings have a finite lifetime, as tribological effects will eventually lead to failure [8]. Cyclic contact stresses generated during the passage of a rolling element, known as rolling contact fatigue (RCF), will result in either surface or subsurface damage. These highly localised stresses, exerted between the bearing raceway and the rolling elements, can be estimated using Hertzian contact theory, assuming there are negligible effects from lubrication [9]. Due to the assumptions of Hertzian contact theory, RCF failure is regarded as a multiaxial fatigue condition, which is much more complicated to study than uniaxial fatigue problems [10].

Failure due to RCF is known to occur in three-phases; (I) shakedown, (II) the steady-state elastic response and (III) instability [11]. It has been established that during shakedown, both the transformation of retained austenite into martensite and work hardening generate small regions of microplasticity, which in turn influence the localised residual stress field [12]. The hardening increases the time spent in steady-state Stage II, where only elastic deformation occurs, without any fatigue damage or accumulation of plastic strain [13]. The duration of Stage II is also influenced by loading conditions, material properties and operating temperature, whilst residual stresses in the material may either reduce or increase during the steady-state stage [14]. Therefore, it can

* Corresponding author.
E-mail address: agpreid1@sheffield.ac.uk (A. Reid).

https://doi.org/10.1016/j.triboint.2019.105893
Received 3 May 2019; Received in revised form 2 August 2019; Accepted 2 August 2019
Available online 02 August 2019

be deduced that increasing the time spent in Stage II will be fundamental to improving the fatigue life of bearings [11]. Gradual material softening causes a reduction of yield strength, eventually triggering the onset of Stage III instability and drastically increasing the size of the plastically deformed region which occurs at the subsurface [15]. The subsurface plasticity causes tensile residual stress to accumulate in the radial direction, perpendicular to the contact surface, increasing the opening force experienced by cracks growing parallel to the surface [16].

Failure arising from RCF has two prominent mechanisms; either subsurface-initiated spalling or surface-initiated pitting [17]. The nucleation and coalescence of subsurface microcracks, most frequently originating at depths corresponding to the maximum shear stress, result in the creation of a spall by detachment of material [18]. In addition to the growth of subsurface plastic deformation, it is hypothesised that RCF subsurface spalling is more prevalent in areas containing non-metallic inclusions, large carbides, voids or other material inhomogeneities [19–21]. On the other hand, surface-initiated pitting is most likely to occur in the presence of surface defects such as dents, which generate regions of substantial stress concentration, nucleating surface cracks that eventually remove small amounts of material [22]. Increased pitting rates have been demonstrated to correlate with higher applied loads, and therefore contact pressures, whilst lubricant conditions were also reported to have a significant influence [23]. It was reported that depth of damage accumulation may also be greatly affected by surface roughness, with spalling becoming notably more prominent as roughness decreased for steel gear systems [24]. It has been demonstrated that bearing life may be enhanced by increasing the probability of damage initiating in the subsurface, opposed to the surface, with approaches such as reducing steel impurities, innovative filtration techniques and improved sealing being researched to lower RCF failure [25].

Whilst RCF explains the finite nature of bearing life, other mechanisms are responsible for the high rates of premature failure in WTG bearings, as their operational life is significantly shorter than the predicted design life based on RCF. Overload events have been proposed as a root cause of the reduced life of WTG bearings [26]. Overloads in WTG bearings can occur due to sudden torque spikes or oscillations through the drivetrain, as a result of exposure to transient wind conditions or shut-downs in normal operation [27]. A wind turbine shutdown can be an emergency measure or a normal operational procedure. Normal shut-downs occur when wind speeds exceed or drop below the most efficient levels for power generation [28]. It has been demonstrated that a cylindrical roller bearing on the HSS can exceed recommended contact stresses by 18% in the event of a manual shutdown [27]. Poor handling and installation can also be responsible for WTG overloads [29]. An overload event can induce subsurface stresses that significantly exceed the yield criterion, producing a region of subsurface plasticity. The extent of subsurface yielding has been evaluated using non-destructive methods such as neutron imaging, indicating that overloads generate more severe plastic deformation than would be expected with typical Stage I RCF [30]. It has been shown that bearing life is significantly reduced by the overload, with failure originating in the subsurface within the plastically deformed region [30]. This suggests that the plasticity induced by overloads decreases the time spent in steady-state Stage II, promoting the early onset of Stage III instability, which results in accelerated damage. An overload could either lead to subsurface originated failure due to gross plastic deformation and the material softening associated with the latter stages of RCF, or surface originated failure, if there were a surface irregularity causing great enough stress concentration effects.

As there are multiple mechanisms contributing to early onset failure, an inherently statistical approach to bearing life prediction models is taken, particularly as knowledge of the components load history is rarely recorded. Equation (1) is the preferred model for calculating the basic life rating, L_{10}, is an estimate for the number of revolutions (in millions) it would take for 10% of bearings to fail under a specified load [31].

$$L_{10} = \left(\frac{C}{P_s}\right)^p \tag{1}$$

where C is the dynamic load rating, P_s is the radial load applied to the bearing and p is the load-life exponent ($p = 10/3$ for cylindrical roller bearings [8]). This paper will focus on the radial bearing load, as it is most relevant, but where necessary, will also refer to the equivalent load applied to the most heavily loaded individual rolling element (P_E), calculated using Equation (2) [32].

$$P_E = \frac{5\,P_s}{Z} \tag{2}$$

In which Z is the total number of rolling elements.

1.2. Strain characterisation using energy dispersive X-ray diffraction

Various synchrotron X-ray diffraction methods have become a powerful tool in determining microscopic elastic strain by measuring the changes in interplanar lattice spacings deep within the materials. Energy dispersive X-ray diffraction (EDXD) uses photons of a wide ranging wavelength spectrum, to measure lattice spacing with a fixed angle detector [33]. Collimation of the incident and diffracted X-rays creates a gauge volume, which is the region where the incident and diffracted beams intersect, such that only diffracted X-rays from within the gauge volume reach the detector [34]. Thus, the EDXD technique can be used to probe inside samples or components. The collimation of the beam, and use of penetrating high energy photons, offers the opportunity to examine subsurface strain in engineering materials, such as steel and aluminium. EDXD experiments regularly involve the characterisation of material residual stress distributions [35] or the mapping of evolving quasi-static strains [36]. In a previous study, Sato et al. used EDXD to analyse residual stress in the ferritic phase of a pearlitic steel wire, whilst simultaneously studying its relationship with dislocation densities [37]. Similarly, Lopez-Crespo et al. performed an in situ experiment using EDXD with digital image correlation (DIC) to map the bulk elastic strain field and surface total strain field, surrounding the crack tip in a bainitic compact tension fatigue specimen [38].

Stroboscopic diffraction techniques allow for ‘live’ strain measurements to be recorded in situ on moving machinery, specifically when the motion is cyclic. The technique requires gating on the EDXD detector's acquisition system. The detector only counts detected X-rays when a digital signal received from an external sensor opens the gate and captures the diffracted beam. The gating sensor is set up so that the gate is only open during a specific point in the motion of the component under investigation. The X-ray counts for one cycle may not be sufficient for forming a full diffraction pattern, but by summing up the collected gated data associated with the same point in the cycle over many cycles, an analysable diffraction pattern is acquired. Baimpas et al. performed such a study, using stroboscopic EDXD to measure strain in the connecting rod of a four-stroke internal combustion engine [39]. A proximity sensor on the engine's output shaft was used to detect when the connecting rod was at the top dead centre position of a stroke, generating a pulsed signal that controlled the X-ray detectors gate, initiating photon counting for a period of time pre-determined by the pulse width. In this case, the width of each pulse from the sensor allowed for 0.289 ms of data collection, resulting in a total of 24 s of data acquisition throughout an 80-min run, which means that 99.5% of incident X-rays were discarded throughout the entire experiment. Mostafavi et al. also used stroboscopic strain measurement techniques, measuring the dynamic strain in the raceway of a rotating ball bearing [40]. A dynamically loaded bearing rig was used to run a bearing. The bearing was fitted with a Hall sensor to provide a triggering system, generating a signal for the detector to collect data for every bearing rotation. With a pulse width of 2 ms and rotational frequency of

150 rpm, the accumulative time required to collect sufficient fitting statistics was 20 s. The experiments demonstrated that reducing the pulse width improved the time-resolution of the dynamic strain measurements, yet it increases the total time required to gather statistically sufficient data, necessary to perform strain analysis. It is also important to reduce the total acquisition time for a single strain measurement when studying the evolution of strain, as it is not possible to distinguish exactly whether a change, such as crack initiation, has occurred in the material. These experiments also highlighted that reducing vibrations in the experimental equipment is essential for improving the accuracy of these techniques, as stroboscopic strain measurements should be collected from a single point within a moving component.

1.3. Aims and structure

The purpose of this work is to (i) develop a stroboscopic technique capable of measuring time-resolved contact strain using EDXD, with optimised time resolution, (ii) map subsurface contact strain distributions for a statically loaded bearing raceway with EDXD, (iii) stroboscopically measure dynamic strain in a pre-overloaded roller bearing. The results of this experiment aim to provide a deeper understanding of the considerable impact severe overload events have on the fatigue life of roller bearings. As developing a technique with the ability to measure in situ strain evolution of a dynamically loaded bearing accurately during a long-term experiment was the primary objective experimental design, a custom-made loading rig was designed for integration with existing hardware and software available on the I12 X-ray beamline at Diamond Light Source [33].

The results include static strain maps and dynamic subsurface strain measurements of an overloaded bearing. Also included are observations of the bearing post-test by destructive sectioning and optical microscopy.

2. Experimental design

2.1. Test bearing

An SKF, NU1010 ECP cylindrical roller bearing was selected for the experiment as it can represent the contact conditions experienced by commercial WTG bearing, yet its geometry is suitably scaled-down to permit adequate X-ray transmission through its raceway. The NU1010 ECP bearing has an outer diameter of 80 mm, a bore diameter of 50 mm and 20 rolling elements [41]. The outer raceway thickness of 16 mm, in the x-direction, permits up to 9% transmission within the 50 keV–150 keV useable X-ray range available on I12. Table 1 provides the chemical composition and of AISI 52100 of which the bearing steel is made [12]. A cylindrical roller bearing was selected as they are frequently found in WTG's. Hertzian contact theory predicts the generation of uniform subsurface stresses along the line of contact, reducing the complexity of the localised strain conditions and allowing for more robust assumptions during data analysis, particularly as experimental setup prevented measurements of the strain component parallel to the line contact.

2.2. Dynamic in situ loading rig

A compact mechanical rig was designed specifically for measuring time-resolved strain in the bearing outer raceway (Fig. 1a and b). The rig was purpose built to allow for measurements in both X-ray and neutron diffraction experiments, taking into consideration the differences in beamline geometry. Neutron data is not reported within this body of work. The load is applied through a threaded bar screw mechanism and cantilever arm. The OMEGA LCM20-20 kN load cell with SGA/A load cell amplifier provided load values as a 0–10 V analogue signal.

To ensure the load is continuously applied along the radial axis, directly on to the region of interest, a line contact was introduced between the cantilever arm and direct loading piece (DLP), as seen in Fig. 1c. The displacement of the DLP was constrained using linear ball bearings, ensuring the load is constantly applied along the radial axis. The shaft diameter (50 mm) is greater where the test bearing is positioned, compared to the main body of the shaft (30 mm) where support bearings are positioned. This prevents obstruction of the X-ray line-of-sight. The custom-made pulley system had the lowest permittable outer diameter for the shaft dimensions, also maintaining a clear line of sight to the region of interest. A 0.75 kW 4 pole single phase motor and WEG CFW-10 inverter were selected, capable of producing the required 2 Nm for a bearing at maximum experimental load. A gear ratio of 1.05:1, provided the greatest transfer of torque possible considering that both the bearing shaft and motor shaft were fitted with pulleys of the lowest feasible pitch diameters. The test bearing was lubricated through the application of KRYTOX GPL 203 grease, operating under mixed-film lubrication regime with a viscosity ratio of 1.79 for dynamic test conditions [42].

2.3. Stroboscopic triggering system

The experiment consisted of two measurement types; static and dynamic. The dynamic measurements required a method to ascertain the position of the rolling elements as a function of time. A stroboscopic triggering system was developed to determine when a roller was in contact with the region of interest. Keyence FU-18 M thru-beam fibre optics were mounted to the rig within a fitted groove in the support bearing housing (Fig. 1d), situated so the transmitted beam passes between the inner and outer raceway. When the bearing rotates the transmitted beam is cut as a passing roller obstructs the line-of-sight between the transmitter and receiver. The Keyence FS-N10 Series digital amplifier with PNP output and in-house signal processing box were used for converting into the required 0–10 V analogue signal. The digital amplifier was calibrated to determine a suitable light intensity threshold, based on the obstructed and unobstructed light intensity. This fibre optic system generated a pulse when the light intensity fell below a specified threshold value, i.e. when the transmitted beam was blocked by a roller.

To assist initial setup of the gating system, a high-speed camera was positioned close to the bearing region of interest and synchronised with the rising edge of pulses emitted from the fibre optic triggering system. This provided a still image each time a pulse was produced, allowing for verification of the time lag required to ensure the roller was in position for X-ray diffraction measurements. To verify the roller position, Phantom 7.3 and MIRO 310 M cameras were used for visible light and X-rays, respectively. Fig. 2 shows a visible light (left) and X-ray (right) image taken using the high-speed camera, synchronised using the trigger pulse and delay to ensure acquisition occurs only when the roller was generating maximum subsurface stress. During dynamic tests the I12 beamline's combined digital signal hardware and field programmable gate array (FPGA), known as ZEBRA, was used to detect the rising edge of the stroboscopic trigger pulse. The ZEBRA was programmed to output a transistor-transistor logic (TTL) pulse with the specified time delay and pulse width to the EDXD detector gate, with data collected only during the width of these pulses.

2.4. EDXD strain measurements

Prior to the experiment, the EDXD detector and collimators were

Table 1
AISI 52100 chemical composition [12].

C	Mn	Si	Cr	Cu	S
0.95–1.10	0.20–0.50	≤0.35	1.30–1.60	≤0.025	≤0.025

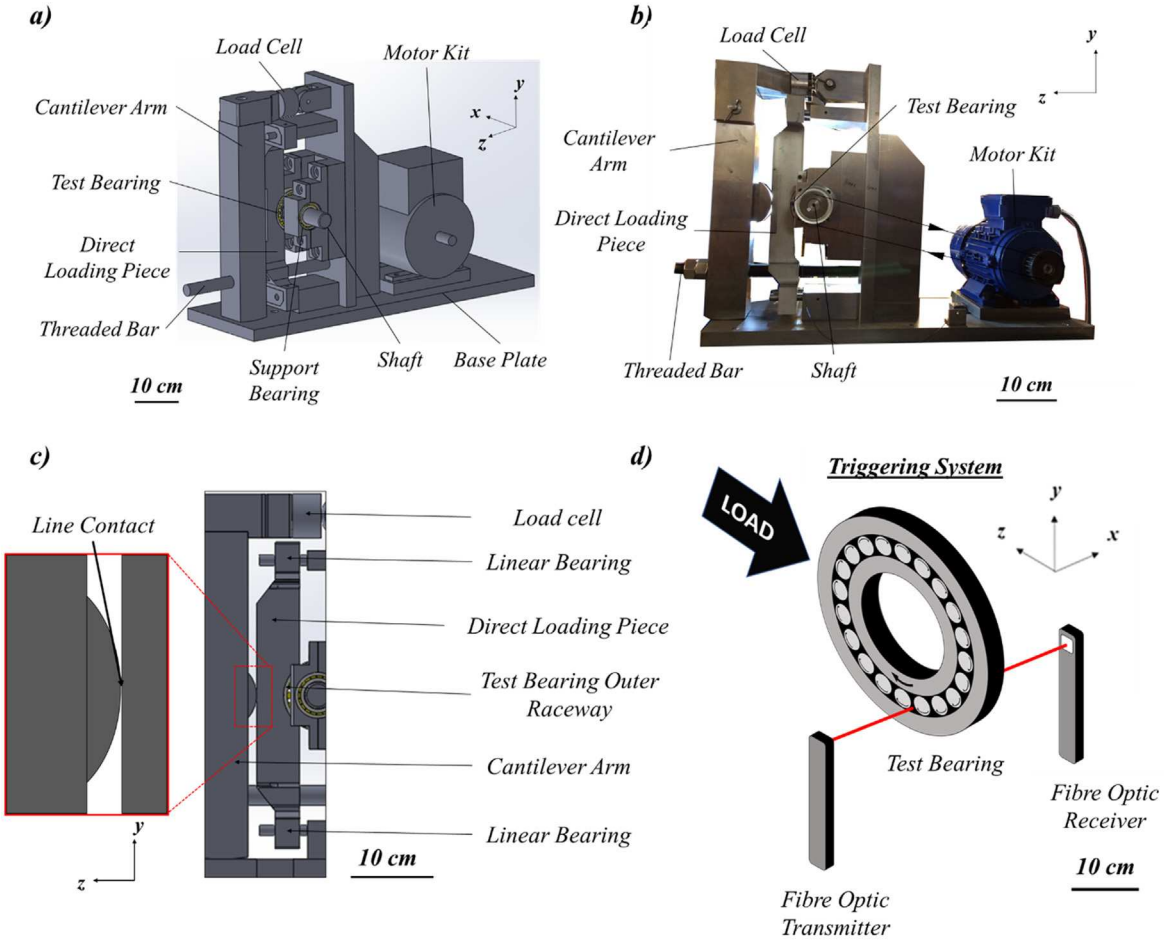

186

Fig. 1. (a) Schematic of the custom-made loading rig. (b) Photograph of the custom-made loading rig. (c) The loading mechanism used to ensure that loads were applied entirely in the radial direction (z-direction). (d) Fibre optic sensors generated a signal for every roller passage, optimising the data acquisition process.

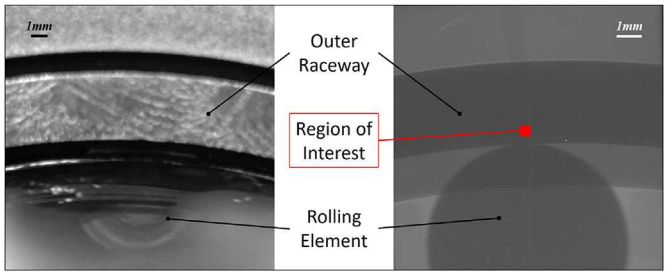

Fig. 2. Images obtained dynamically when the pulse was synchronised with the roller position. (Left) Visible light image. (Right) X-ray radiograph.

aligned with the X-ray beam, and a calibration of intensity versus the reciprocal lattice vector, q, was obtained using a National Institute of Standards (NIST) 674b cerium oxide reference sample. A straight forward relationship between q and the atomic lattice spacing d in a material is given by:

$$q = \frac{2\pi}{d}$$

The test rig was mounted on the I12 sample stage that is used to accurately position the bearing region of interest within the X-ray beam line-of-sight. The sample stage can be translated in the x-, y- and z-directions, with a resolution on 10 μm [33]. To align the test sample and detector, the rig was positioned so that the incident beam was parallel to the axial direction, through the test bearing (x-axis). An approximate alignment of the X-ray beam and outer raceway region of interest was initially completed using a laser. Refinement of the necessary y- and z-sample stage positions was then performed using the high-speed MIRO 310 M (CMOS) camera with transmitted X-rays being converted to visible light using a scintillator. For static tests a script translated the stage to a set point required to generate a map around the localised contact stresses. Mapping of the subsurface strain in the contact region under static conditions was performed by scanning a $1.5 \times 0.9\,mm^2$ region directly beneath the contact, with point intervals every 150 μm. The scan time for all 77 points was 120 s each. For the dynamic tests the camera was used to determine the y- and z-positions so that the centre of the gauge volume was located at 250 μm radially from the subsurface (see Fig. 3a and b). For dynamic scans the incident beam geometry was 150 × 150 μm with a gauge volume length of approximately 5 mm along the line of contact. To align the gauge volume in the x-direction, a scan was taken whereby the stage was translated parallel to the incident beam. The intensity of diffracted X-rays was plotted as a function of displacement in the x-direction, with intensity dropping when the gauge volume was no longer entirely located within the sample. By noting the stage positions, where the gauge volume had entered and exited the bearing, it was possible to determine the location corresponding to the centre of the sample. All experimental loads were applied radially along the z-direction.

The I12 EDXD detector has 23 detecting elements set at $2\vartheta \cong 4.5^\circ$, equally spaced through azimuthal angles of 0°–180°, with 8.18° between each element. To determine the dynamic fatigue load, it was decided that maps would be taken of the statically loaded bearing, and the load was chosen where the Hertzian contact stresses were clearly visible in the map. By ensuring that subsurface stress was significant

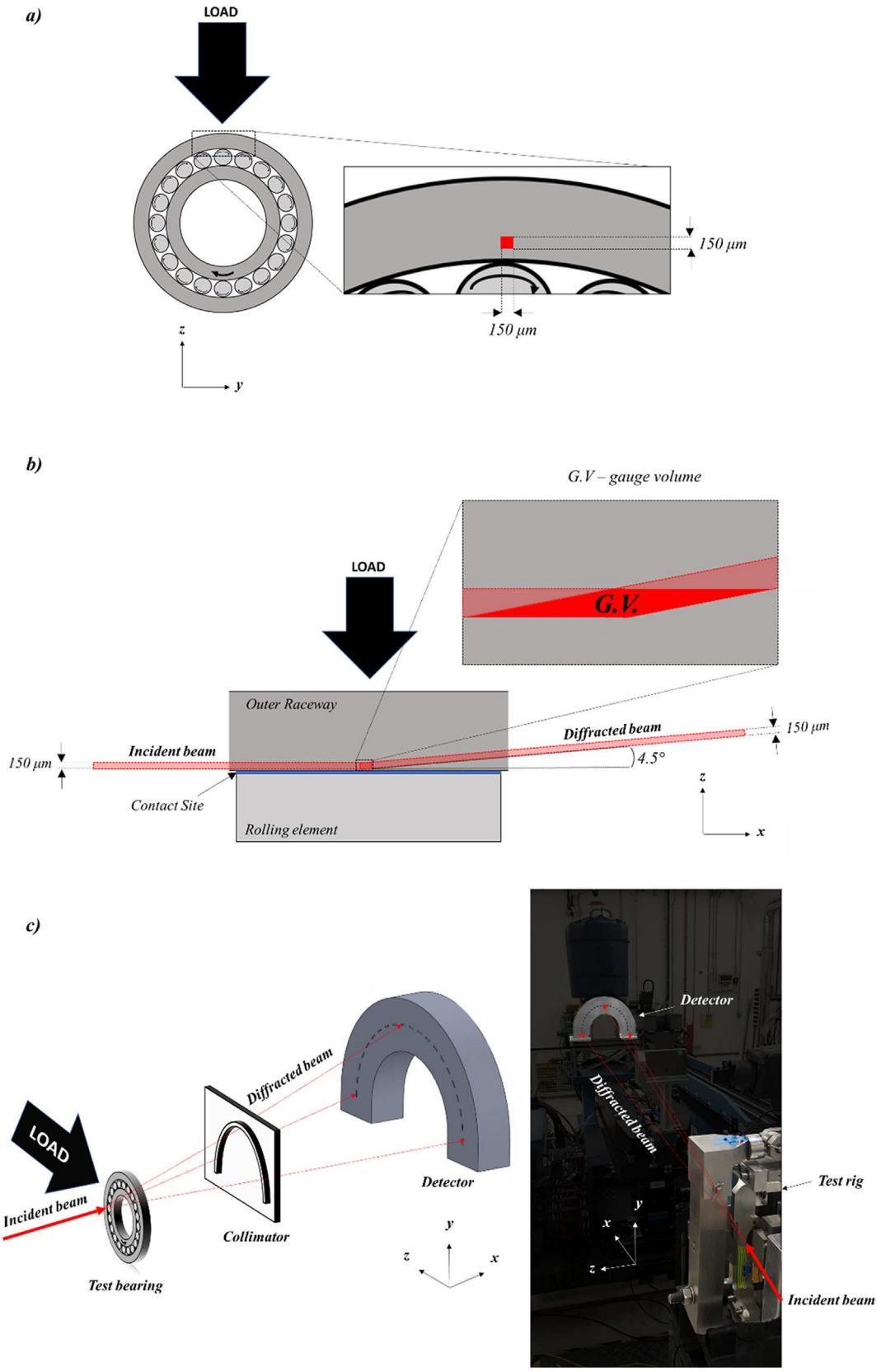

Fig. 3. a) Projection of the gauge volume in the yz-plane position of the outer raceway, relative to the rolling element and radial load application. The centre of the gauge volume was 250 μm into the subsurface, within a region plastically deformed from pre-overloading. b) Projection of the gauge volume in the xz-plane. c) (Left) Schematic of EDXD experimental setup, with applied load direction (z-direction), collimator, and 23-element detector. (Right) Photograph of experimental setup prior to alignment of the collimator. The image has been darkened where auxiliary equipment is positioned, making the detector and test rig more visible.

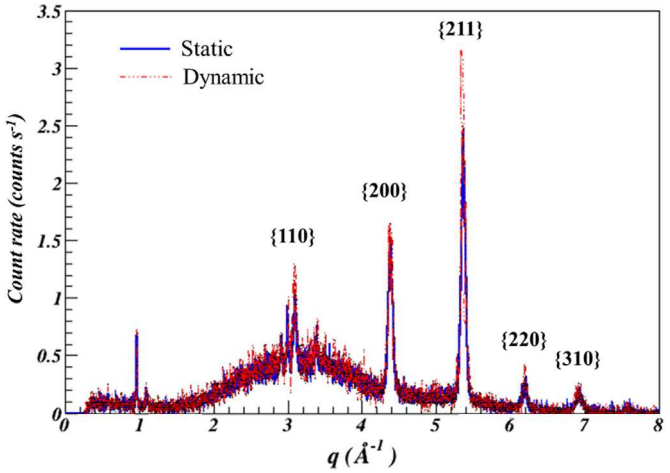

Fig. 4. Diffraction spectra for a static and dynamic scan, with labelled {hkl} planes.

enough to be visualised in static conditions, it was deemed suitable for dynamic experiments. See Results Section 3.1 for static stress maps. Static measurements were performed with a rolling element positioned at the region of interest, applying pressure to the raceway in the area covered by the scan.

The stroboscopic tests completed on I12 measured strain at a single location, whereas static tests were used to generate 2D maps of the subsurface strain profile. Three dynamic scans were performed for the same loads performed for static scans and it was determined that a cumulative 60 s data acquisition time provided sufficient fitting statistics. It took approximately 13 min to collect each 60 s data point, with a pulse width of 500 μs and a rotational frequency of 854 rpm, typical of a WTG intermediate-speed shaft (ISS) bearing with a HSS gear ratio of 2:1 [44,45]. Fig. 4 compares the diffraction spectra for a static scan and a dynamic scan, demonstrating the quality of data is not compromised by using the stroboscopic technique. Analysis of the diffraction data was carried out using the pyXe strain analysis software [43], with a Rietveld type (Pawley) refinement being used to determine the lattice parameter for each of the 23 detectors. While the focus was on radial strain, leveraging the measurements from each detector to calculate the in-plane strain tensor improves the overall measurement accuracy. In this case, the uncertainty (standard deviation) in strain from the in-plane strain tensor fit was $\pm 7 \times 10^{-5}$, which is associated with an error in stress of approximately ± 14 MPa.

2.5. Finite element analysis

A three-dimensional elastic-plastic finite element model, developed in ABAQUS version 6.14–2 [46] and validated in previous work [30], was used to simulate static loading conditions for comparison with those measured using EDXD. Fig. 5 shows a schematic of the model and boundary conditions. The bearing raceway and rolling element used quadratic elements (C3D20R), whilst the other components were rigid bodies, modelled using bilinear rigid quadrilateral elements (R3D4). Mesh refinement in the contact region was performed to give elements with dimensions 150 × 150 μm in the yz-plane, matching the dimensions as the X-ray gauge volume. A quarter of the bearing was modelled as the x-axis and ϑ-axis (accounting for bearing curvature) were assumed to be symmetric, whilst friction in the contact site was ignored. Quasi-static conditions were used in the simulations, with an assumption of isotropic hardening using the stress-strain curve for AISI 52100 [47]. The model was used to predict subsurface elastic strains in static loading conditions, with material properties found in Table 2.

3. Results

3.1. Static strain mapping

Strain was mapped under static conditions with the roller placed directly beneath the contact site. The load was progressively increased from 3.6 kN to 9.0 kN in increments of 1.8 kN, with elastic strain maps being generated concurrently, to allow for visualisation of localised subsurface radial strain distributions. Fig. 6 demonstrates the subsurface radial strain distributions measured using EDXD. Above 5.4 kN the strain distributions resembled those expected by Hertzian contact theory, yet below it was not possible to distinguish any recognisable strain distributions. A load of approximately 9.0 kN was deemed as suitable for running the dynamic tests on an overloaded bearing, as the map demonstrated that at this load the subsurface strain distributions are great enough to be detected within a dynamic gauge volume of 150 × 150 μm, at 250 μm beneath the contact subsurface. This corresponds to a maximum contact pressure of approximately 1350 MPa, in between the maximum allowable stresses of 1300 MPa for HSS bearings and 1500 MPa for low speed planetary bearings, as reported in wind turbine design standards [27].

The experimentally measured subsurface radial strain at 9.0 kN demonstrates a similar trend to the FEA at the same load, although measured strain values are of lower magnitude. Fig. 7 shows a comparison of the FEA and experimental radial strain, with a plot of values from the contact into the subsurface. Although spatial alignment errors are small when using the precise positioning equipment on I12, the nature of the localised contact strains suggests that the apparent shift in strain could be caused by a small misalignment, with the dashed lines showing the minimum and maximum FEA values if a misalignment as small as the height of the gauge volume, 150 μm, had occurred in either direction along the z-axis.

3.2. Time-resolved subsurface elastic strain measurements

Prior to beginning the 24-h time-resolved test, individual data points were measured dynamically at different loads. Each scan cumulatively acquired 1 min of data, with three scans performed at each load. Fig. 8 demonstrates the measured elastic strain for three scans at each loading condition, confirming the technique's capability to measure time resolved strain and that approximately 9.0 kN was a suitable load for the long-term dynamic test. It was not possible to run a dynamic test at 0.0 kN as a load is required to ensure the outer raceway remains static, nonetheless results show that below roughly 5.0 kN it is difficult to differentiate the strain from the noise of the detector. This was equally demonstrated in the static maps, suggesting that below a threshold load, strain cannot be measured. The d_0 value used for the dynamic test was the same as that of the static maps.

As a principal aim of the project is to explore the influence of yield inducing overloads on subsurface fatigue strains, the dynamic test specimen was subject to an overload event prior to cycling. The details of the apparatus with which the overload is applied is given elsewhere [30]. However, to ensure the current work is self-contained, a brief description of the apparatus and overload procedure is given here. The overload was performed using a purpose-built loading frame, applying a load to the bearing outer raceway using a single rolling element. A cage was designed to hold an isolated bearing outer raceway, whilst a fork was used to carry a static shaft for holding the individual rolling element through the middle of the raceway. The rolling element was positioned at the region of interest and an Instron loading frame was used to pull the fork in tension, applying the designated load to the contact site. The rolling element was discarded after the overload was performed, with only unloaded elements being used for the dynamic X-ray experiment. Previous work indicated that the elastic limit being reached at 40 kN, with a 136 kN overload (P_E = 34 kN) seeding a plastic zone that initiates in the subsurface and propagates to the

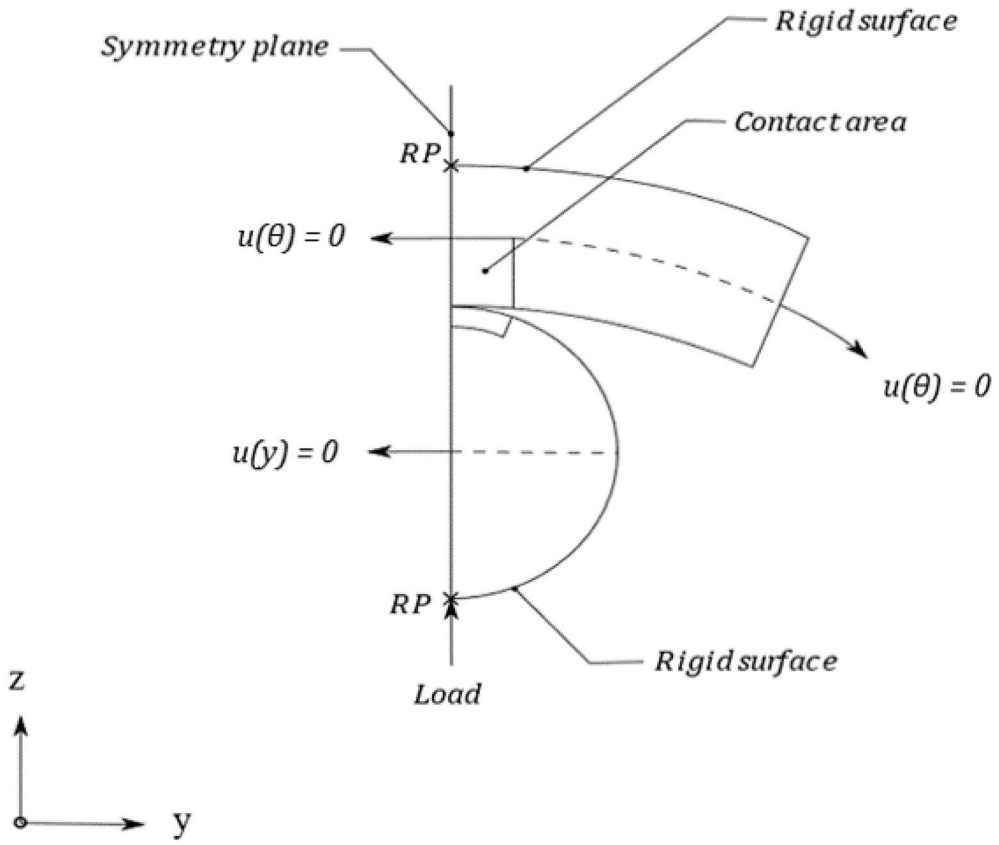

Fig. 5. Schematic of finite element model, with labelled boundary conditions.

Table 2
AISI 52100 properties [48].

Property	Symbol	Value
Density [Kg/m3]	ρ	*7827*
Young's Modulus [GPa]	E	*201.33*
Poisson's ratio	ν	*0.3*
Yield Stress [MPa]	σ_Y	*1410.17*

contact surface [30]. As the long-term test was being run at fatigue load of 8.8 kN, a more significant pre-fatigue overload event of 180 kN was used (P_E = 45 kN). This load was chosen to increase the probability of damage initiation within the available experimental timeframe at a lower cyclic load than had been presented in previous studies, whilst also increasing the likelihood that dynamic measurements were taken from a plastically deformed region. The test was run for 23 h and 35 min, equating to approximately 1.21 million bearing revolutions at 854 rpm, approximately 0.5% of the L_{10} life, as predicted using equation (1). A beam loss in the synchrotron storage ring between 12 and 14 h left a gap in data acquisition.

Fig. 9 shows the plot of subsurface radial strain averaged within the gauge volume, at a depth of 250 μm beneath the contact. Over the duration of the experiment, the strain became increasingly compressive throughout cycling, possibly due to continual material softening in the region being measured as a result of early onset Stage III RCF caused by the significant pre-cycling overload event. Scatter in the strain measurements predominantly fits within the experimental uncertainty of ± 70 με. Additionally, small amounts of scatter may be attributed to the continual variation of subsurface strain, including whilst data was being collected during the gating pulse width. The compressive radial strain in this region increases by approximately 19% during bearing operation. This is of interest as the elastic properties of the localised subsurface and surface region appear to continually alter when cycling is nested within a plastically deformed region. The induced subsurface residual stress field clearly influences the cyclic elastic strains as they are more than double those for the static scans when the specimen had not been subjected to an overload. In many cases the purposeful induction of residual stresses has been utilised to improve component life, yet the severity of the plastic deformation appears to accelerate damage, as discussed in Section 3.3.

3.3. Post-fatigue interrogation

A final static map was performed on the bearing post-cycling, with the dynamic load applied and a roller positioned beneath the surface. The map shows a significant tensile region in the subsurface, slightly offset from the contact zone. Fig. 10 shows a comparable subsurface tensile region is also apparent in the FEA, demonstrating that the overload is inducing a significant residual stress field in the material. A profile of radial elastic strain into the subsurface provides reasonable agreement between the FEA and experimental data. The FEA map suggest a compressive region should be present at the surface, which is not visible in the experimental map. This could be an effect of the previously mentioned possibility of misalignment, or that the self-equilibrating residual stress field generated during the overload varies from the FEA at the surface due to the inherent stresses that were already present in the bearing prior to the influence of any experimental loading.

3.4. Post-fatigue optical microscopy

The bearing was sectioned circumferentially to verify whether a failure had occurred. A bearing is considered to have failed is when it no longer functions as intended, as opposed to being completely non-operational [49]. At the end of the fatigue test, the bearing appeared to be fully operational, without presenting obvious indications of failure,

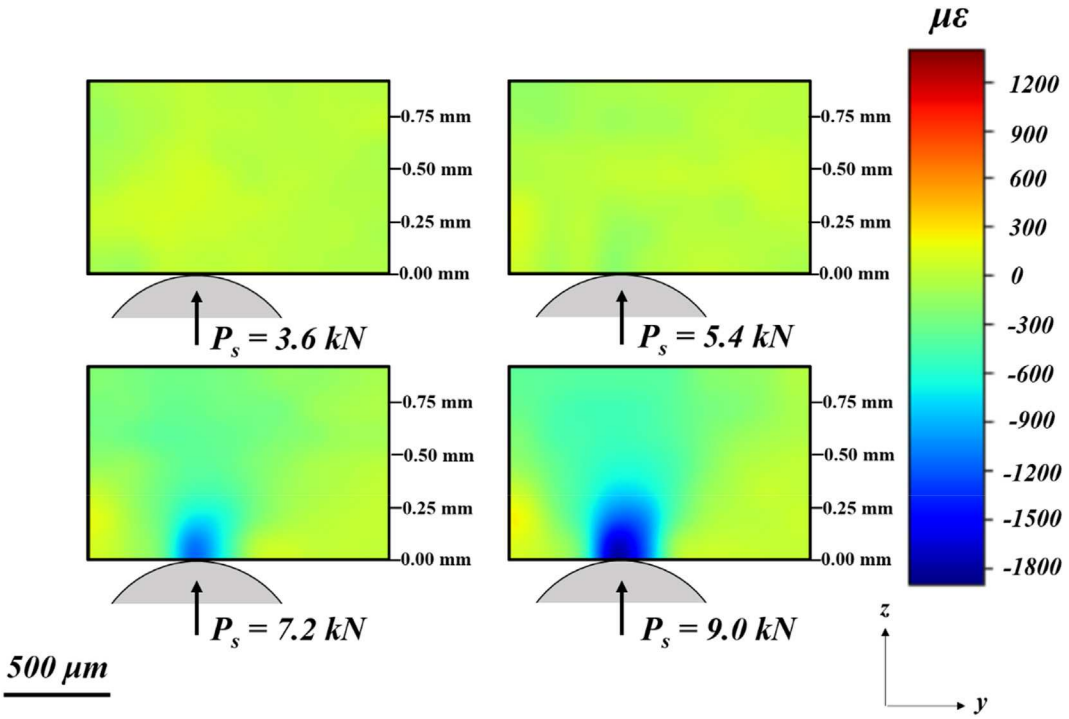

Fig. 6. Two-dimensional subsurface radial strain maps (ε_{zz}) at loads of P_s = 3.6 kN, 5.4 kN, 7.2 kN and 9.0 kN. The subsurface depth axis has been included.

yet optical microscopy of the sectioned raceway revealed the presence of cracking, and the appearance of severe deformation in the contact region, as seen in Fig. 11. Cracks were observed beneath the contact zone, most notably a crack running roughly 4 μm into the subsurface, classified as a surface failure. The observed cracks are indicative of fatigue pitting and occurred within a highly deformed region with width and maximum depth of roughly 210 μm and 20 μm, respectively. As suggested in the literature, surface irregularities introduced by a substantial overload generate regions of high stress concentration resulting in surface initiated cracking, which may have contributed towards the observed surface damage in this sample [22].

4. Discussion

Using the hardware and software developed as part of this project, the ability to measure time-resolved strain has been successfully demonstrated. The custom-designed rig and experimental setup allowed for high quality data acquisition, and long-term dynamic testing allows for the measurement of in situ subsurface strain evolution. Fibre optic sensors to detect the passage of every rolling element in the bearing has proven effective, optimising the data acquisition time for a single strain measurement when compared to previous studies [40]. Static maps provide a useful validation on that contact stress distributions correspond closely those predicted by Hertzian contact theory. The long-term dynamic tests demonstrate increase radial strain with time, suggesting that when cycling occurs nested within the yield zone, material softening causes accelerated failure.

Experimental results provide further evidence that overloads that seed subsurface plastic regions contribute towards premature failure of wind turbine gearbox bearings. The comparison of FEA and experimental radial elastic strain mapping have clearly demonstrated that substantial overloading generates a residual stress field in the region in the location of fatigue loading occurs during bearing operation. The tensile residual stress gradients are positioned where the highly localised cyclic fatigue stresses occur, reducing the expected time for failure by driving crack growth parallel to the surface. This work supports literature suggesting that, although the effect of subsurface residual stress and plastic deformation contribute towards failure, the presence of tensile residual stress in the radial direction increases the force driving crack growth [16]. The observed crack appears to be a precursor to fatigue pitting, which eventually lead to more severe surface failures, as described by in other work by Muro et al. [22]. Without an overload event, the bearing would still be expected to fail due to rolling contact fatigue once the steady-state Stage II has progressed to Stage III instability, yet the results support the hypothesis that a gross plastic overload effectively accelerates the onset of Stage III instability and material softening, resulting in premature failure.

It appears that the damage arises from work cycling within a region of severe plastic deformation, caused by the overload event. The width of the damaged region was experimentally measured at 218 μm (See Fig. 11), similar to the plastic zone predicted by Hertzian contact theory, which has a width of 210 μm, at the dynamic load of 8.8 kN. If the damage were to be solely attributed to static overloading of 45 kN, the damaged region would have been more comparable with the overloading contact width of 951 μm, assuming a Hertzian contact at 180 kN. The dimensions of the presented deformation correlate much more closely with those predicted at the lower dynamic load, opposed to the much higher overload, suggesting that whilst the overload accelerates the extent of damage, rolling contact fatigue remains the primary failure mechanism. Whilst inherent material defects contribute towards premature failure, overloading appears to bridge the influence of existing material flaws or seed defects that negatively impact bearing life.

The same argument presented above on the comparable damaged zone width and plastically deformed region during the dynamic load can put forward in terms of subsurface depth. Dynamic loads (i.e. 8.8 kN) used during the experiment generate a maximum subsurface shear stress at 83 μm from the contact site, based on the Hertzian contact model. The overload carried out before the experiment at 180 kN, induces subsurface plastic deformation with a significantly larger geometry and a maximum shear stress at 370 μm deep from the contact point. The observed damage, as can be seen in Fig. 11, occurred between the surface and a subsurface depth of 20 μm which is more comparable with the effect expected from the dynamics load than the

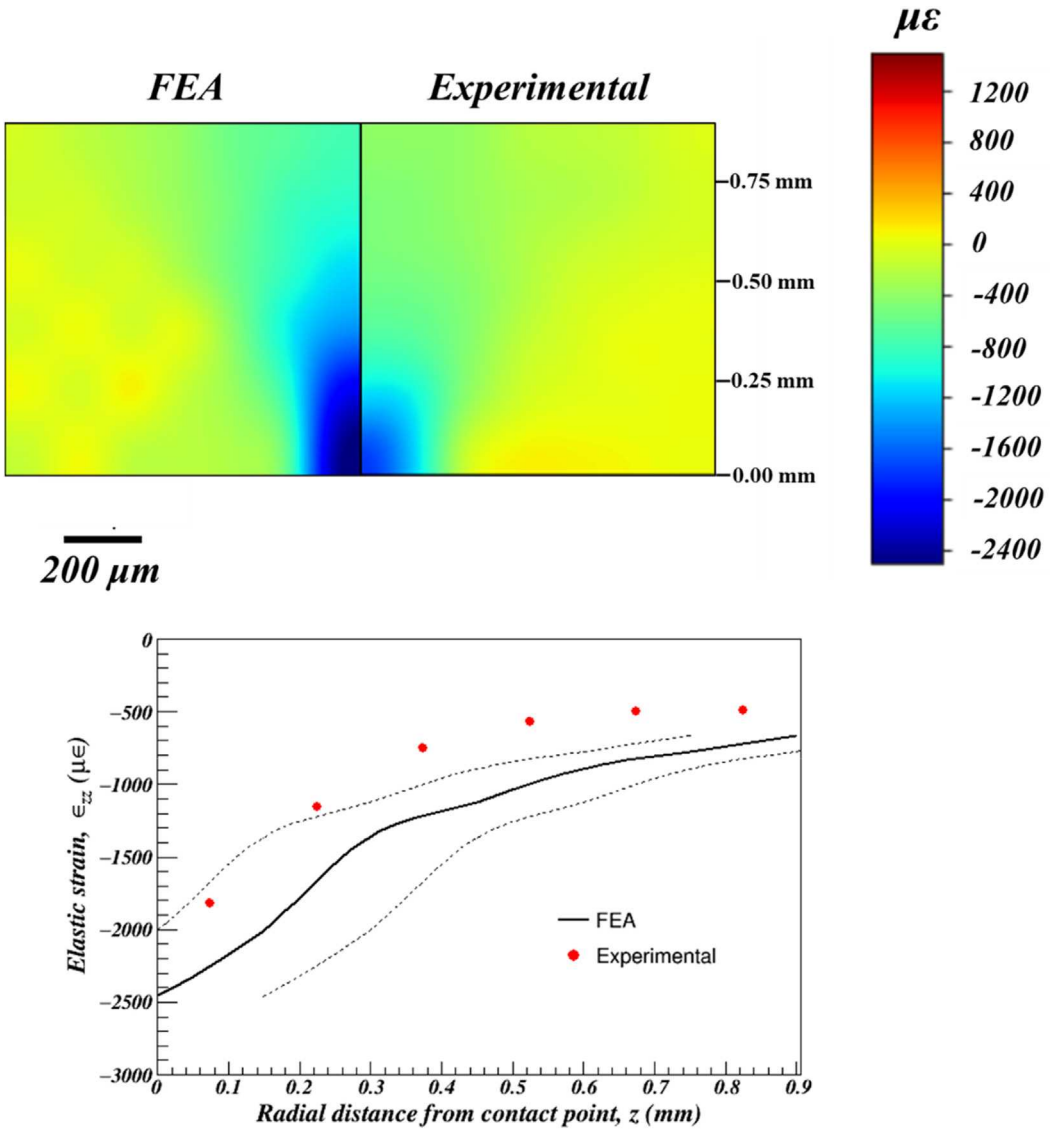

Fig. 7. (Top) Radial elastic strain map at 9.0 kN compared with FEA results at the same load. (Bottom) Radial elastic strain as a function of distance from the contact site. The dashed lines represent the minimum and maximum values when taking into consideration a misalignment of up to 150 μm.

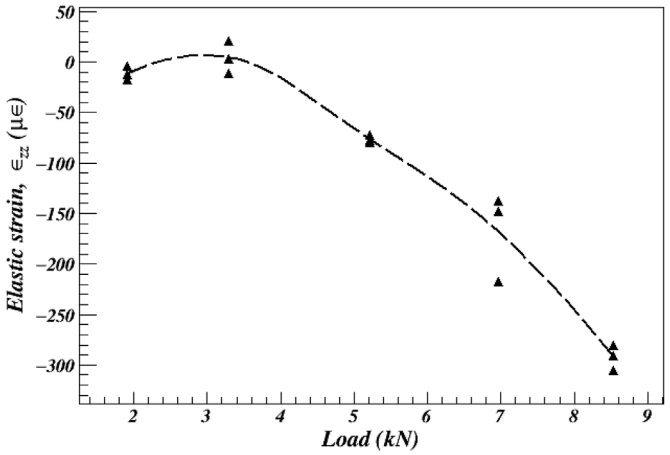

Fig. 8. Radial elastic strain (ε_{zz}) measured stroboscopically for three scans performed at each load. The dashed line is a fit of the average strain for each load.

overload. Fig. 12 demonstrates the comparative sizes of the surface defect, subsurface maximum principal shear stresses at the dynamic load, as predicted by Hertzian contact theory, and a section of the subsurface plastic zone induced through overloading, as predicted by FEA. It should be noted that the contours and plastic zone has been cropped to allow for suitable comparison with the surface defect. The previous study by Reid et al. [30] demonstrated premature bearing failure within a region of gross plastic deformation generated by a severe overload event. This work supports the hypothesis that a yield inducing overload may significantly reduce bearing life expectancy.

It is apparent that the plastic zone's size should encompass the localised region of maximum dynamic stress, yet it can also be postulated that the location of damage is dependent on the magnitude of fatigue loading rather than the overload, assuming the dynamic stresses fall within the yielded region. This implies, such as for this experiment, that an overload generating surface and subsurface plasticity followed by relatively low fatigue loads fail at the surface. For future experiments, it would be beneficial to perform thorough characterisation of the surface condition post-overload, but prior to dynamic testing. This would provide greater understanding of the extent of surface damage from the overload event, potentially supporting the proposal of an exact failure mode. Also, the presence of inherent material defects and impurities

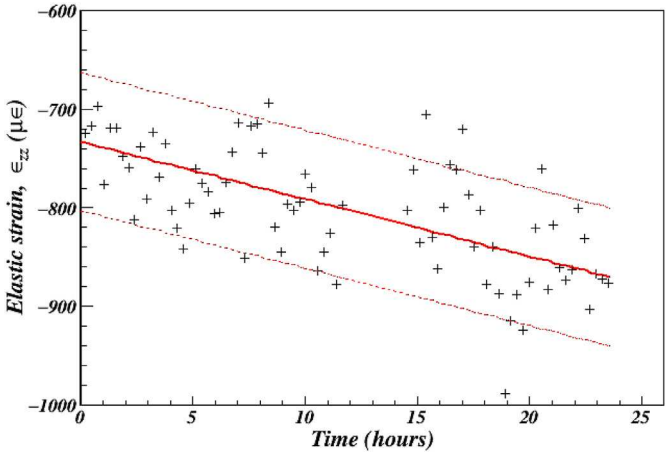

Fig. 9. Time-resolved subsurface radial elastic strain (ε_{zz}) measured during the long-term dynamic test at 8.8 kN having been exposed to overload equivalent to P_s = 180 kN. The experimental uncertainty of ± 70 με has been represented using a line of best fit (solid red line), with minimum and maximum errors (dashed red lines). A gap in the data between 12 and 14 h was due to loss of stored beam in the synchrotron. (For interpretation of the references to colour in this figure legend, the reader is referred to the Web version of this article.)

will also impact mechanisms responsible for failure, yet their role in life reduction has not been considered for this research.

With the development of this novel and effective technique for measuring subsurface strain, future experiments can be planned to further understand the influence of subsurface stresses on rolling contact fatigue failure. For example, the completion of tests with varying overloads and operational loading conditions would allow for further validation of the hypothesis that surface and subsurface failure is determined solely by fatigue load, rather than the extent of subsurface plastic deformation. This would also provide a more in depth understanding of precisely how overload events impact bearing life. Having extended experimental times would allow for longer dynamic experiments to be completed, yet beamtime on synchrotron sources is usually limited to a few days. Improved knowledge about the effect of overloads and extent of life reduction has the potential to be scaled up and theoretically could be used to predict the life of in-service wind turbine

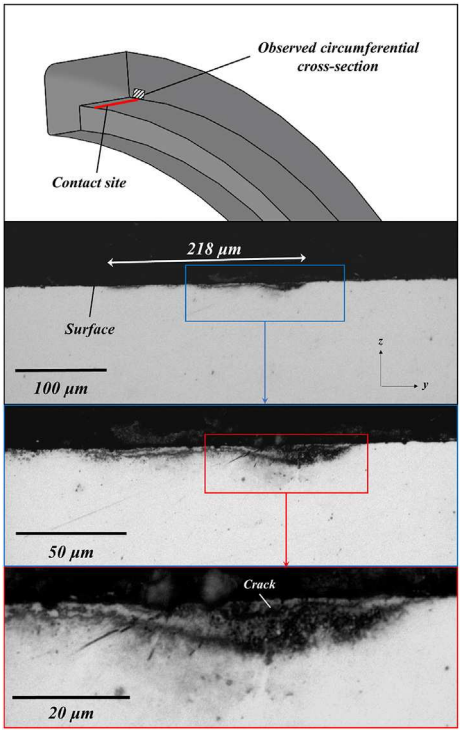

Fig. 11. Schematic to demonstrate the circumferential cross-section surface being observed, with visible light micrographs taken from the contact site at x20, × 50 and × 100 magnification.

gearbox bearings, if their load history has been recorded. The rig could be optimised for future experiments, for example, although load variation throughout the dynamic test was below 4%, a feedback loop could be installed to ensure the applied load is constant.

4.1. Future work: stroboscopic neutron diffraction

The rig has been specifically designed for the completion of X-ray and neutron diffraction experiments. Now that this technique has been successfully demonstrated using energy dispersive X-ray diffraction, the

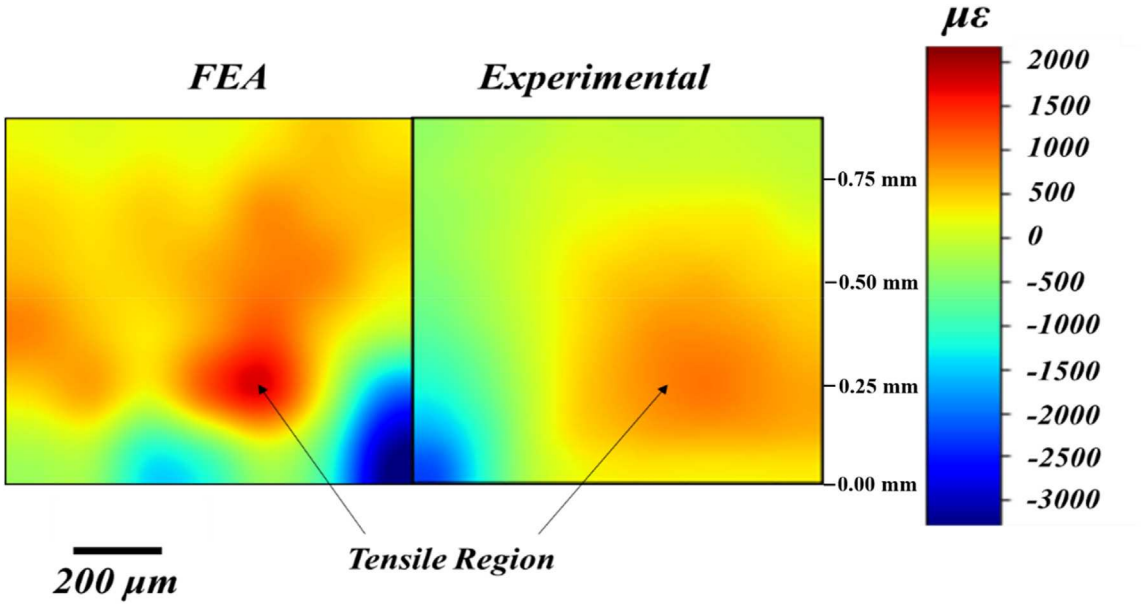

Fig. 10. Radial elastic strain FEA results for bearing a bearing exposed to a bearing pre-overloaded at P_E = 45 kN and static load of P_s = 8.8 kN, compared with the experimental radial elastic strain map of a bearing pre-overloaded at P_E = 45 kN and fatigued for approximately 531,000 cycles at P_s = 8.8 kN.

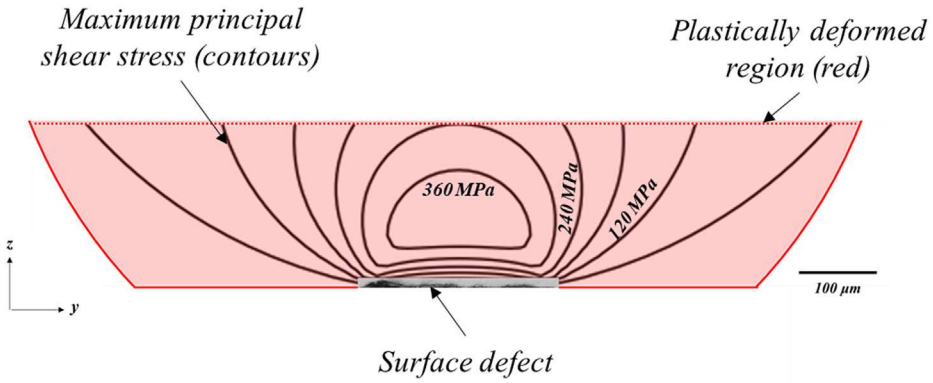

Fig. 12. Comparative sizes of the surface defect, subsurface shear stress contours as predicted by Hertzian contact theory, and subsurface plasticity caused by the overload. The optical micrograph is at x20 magnification. The shear stress contours and plastically deformed region has been cropped to allow for reasonable comparison with the defect, as its dimensions are significantly smaller than the other features.

main aim is to perform this experiment using neutron diffraction. This experiment is part of a wider project to develop the ability for time-resolved strain measurements on the world-renowned strain diffractometer, ENGIN-X at ISIS neutron source, UK. The instrumentation on I12, whilst demonstrating unrivalled spatial resolution and rapid data acquisition times, only allows for stroboscopic data acquisition at times that coincide with the pulses, i.e. at only one point within a single fatigue cycle determined the length of which is determined by the pulse width. It is therefore not possible to study the cyclic stress induced by rolling contact fatigue. ENGIN-X can collect all incident neutrons and therefore offers the unique opportunity to measure the strain evolution throughout the entire fatigue cycle. Also, neutrons can penetrate much greater depths of engineering material, such as steel, meaning that if it were possible to transition this technique to ENGIN-X, much larger tests samples could be studied, including commercial wind turbine gear box bearings. There are currently obstacles to this transition due to much slower data acquisition times and worse spatial resolution. The next phase in assisting transition of the presented technique are to ensure that data acquisition hardware and analysis software capable of accurate strain measurements.

5. Conclusions

- The use of a custom-made rig and fibre optic triggering system allows for measurement of time-resolved elastic strain using energy dispersive X-ray diffraction. The data acquired during both static and dynamic scans is of similar quality.
- A long-term 24-h stroboscopic scan demonstrated a gradual increase of compressive radial strains in an overloaded region of the bearing outer raceway.
- Overloading accelerates the onset of Stage III instability, reducing bearing life and increasing the probability of cracking due to rolling contact fatigue.

Data availability

All data is available with the corresponding author and provided upon request.

Acknowledgments

The authors are grateful for the Diamond Light Source beamtime (experiment number EE18468-1), whilst A Reid would like to acknowledge EPSRC, United Kingdom and STFC, United Kingdom for their support through the sponsored PhD programme (Grant number: EP/M508135/1). A Reid would also like to thank David Butcher (University of Sheffield) for manufacturing the dynamic loading rig.

References

[1] Helsen J, Guo Y, Keller J. Experimental investigation of bearing slip in a wind turbine gearbox during a transient grid loss event. Wind Energy 2016;19:2255–69. https://doi.org/10.1002/we.
[2] Spinato F, Tavner PJ, Van Bussel GJW, Koutoulakos E. Reliability of wind turbine subassemblies. IET Renew Power Gener 2009;3:387–401. https://doi.org/10.1049/iet-rpg.2008.0060.
[3] Chengbing H, Xinxin F. Institutions function and failure statistic and analysis of wind turbine. Phys Procedia 2012;24:25–30. https://doi.org/10.1016/j.phpro.2012.02.005.
[4] Sheng SS. Gearbox reliability Database : yesterday, today, and tomorrow. Chicago, Illinois: NREL, Wind Turbine Tribology Seminar; 2014.
[5] de Azevedo DHM, Araújo AM, Bouchonneau N. A review of wind turbine bearing condition monitoring : state of the art and challenges. Renew Sustain Energy Rev 2016;56:368–79. https://doi.org/10.1016/j.rser.2015.11.032.
[6] Guo Y, Keller J, LaCava W. Planetary gear load sharing of wind turbine drivetrains subjected to non-torque loads. Wind Energy 2015;18:757–68. https://doi.org/10.1002/we.
[7] Mandic G, Member S, Nasiri A, Member S, Muljadi E, Oyague F. Active torque control for gearbox load reduction in a variable-speed wind turbine. IEEE Trans Ind Appl 2012;48:2424–32. https://doi.org/10.1109/TIA.2012.2227131.
[8] Harris TA, Barnsby RM. Life ratings for ball and roller bearings. Proc Inst Mech Eng J J Eng Tribol 2001;215:577–95.
[9] Evans M. An updated review : white etching cracks (WECs) and axial cracks in wind turbine gearbox bearings. Mater Sci Technol 2016;32:1133–69. https://doi.org/10.1080/02670836.2015.1133022.
[10] Gegner J. Tribological aspects of rolling bearing failures. IntechOpen: Tribol. – Lubr. Lubr.; 2011. p. 33–94. https://doi.org/10.5772/873.
[11] Sadeghi F, Jalalahmadi B, Slack TS, Raje N, Arakere NK. A review of rolling contact fatigue. J Tribol 2009;131. https://doi.org/10.1115/1.3209132. 041403.
[12] Bhadeshia HKDH. Steels for bearings. Prog Mater Sci 2012;57:268–435. https://doi.org/10.1016/j.pmatsci.2011.06.002.
[13] Bhattacharyya A, Subhash G, Arakere N. Evolution of subsurface plastic zone due to rolling contact fatigue of M-50 NiL case hardened bearing steel. Int J Fatigue 2014;59:102–13. https://doi.org/10.1016/j.ijfatigue.2013.09.010.
[14] Turteltaub SÃ, Suiker ASJ. Transformation-induced plasticity in ferrous alloys. J Mech Phys Solids 2005;53:1747–88. https://doi.org/10.1016/j.jmps.2005.03.004.
[15] Voskamp AP. Material response to rolling contact loading. J Tribol 1985;107:359–64.
[16] Voskamp AP, Mittemeijer EJ, Voskamp AP, Mittemeijer EJ. State of residual stress induced by cyclic rolling contact loading State of residual stress induced by cyclic rolling contact loading. Mater Sci Technol 2013;13:430–8. https://doi.org/10.1179/mst.1997.13.5.430.
[17] Warhadpande A, Sadeghi F, Evans RD. Microstructural alterations in bearing steels under rolling contact fatigue part 1-Historical overview. Tribol Trans 2013;56:349–58. https://doi.org/10.1080/10402004.2012.754073.
[18] Slack T, Sadeghi F. Explicit finite element modeling of subsurface initiated spalling in rolling contacts. Tribol Int 2010;43:1693–702. https://doi.org/10.1016/j.triboint.2010.03.019.
[19] Warhadpande A, Sadeghi F, Kotzalas MN, Doll G. Effects of plasticity on subsurface initiated spalling in rolling contact fatigue. Int J Fatigue 2012;36:80–95. https://doi.org/10.1016/j.ijfatigue.2011.08.012.
[20] Al-Tameemi HA, Long H, Dwyer-Joyce RS. Initiation of sub-surface micro-cracks and white etching areas from debonding at non-metallic inclusions in wind turbine gearbox bearing. Wear 2018;406–407:22–32. https://doi.org/10.1016/j.wear.2018.03.008.
[21] Gould B, Greco A, Stadler K, Xiao X. An analysis of premature cracking associated with microstructural alterations in an AISI 52100 failed wind turbine bearing using X-ray tomography. Mater Des 2017;117:417–29. https://doi.org/10.1016/j.matdes.2016.12.089.
[22] Muro H, Tsushima T, Nagafuchi M. Initiation and propagation of surface cracks in rolling fatigue of high hardness steel. Wear 1975;35:261–82. https://doi.org/10.1016/0043-1648(75)90075-7.
[23] Zhou Y, Zhu C, Gould B, Demas NG, Liu H, Greco AC. The effect of contact severity

on micropitting : simulation and experiments. Tribol Int 2019;138:463–72.
[24] Liu H, Liu H, Zhu C, Zhou Y. A review on micropitting studies of steel gears. Coatings 2019;9:1–27. https://doi.org/10.3390/coatings9010042.
[25] El Laithy M, Wang L, Harvey TJ, Vierneusel B, Correns M, Blass T. Further understanding of rolling contact fatigue in rolling element bearings - a review. Tribiology Int 2019;140:105849. https://doi.org/10.1016/j.triboint.2019.105849.
[26] Evans MH. White structure flaking (WSF) in wind turbine gearbox bearings: effects of 'butterflies' and white etching cracks (WECs). Mater Sci Technol 2012;28:3–22. https://doi.org/10.1179/026708311X13135950699254.
[27] Long H, Dwyer-Joyce RS, Bruce T. Dynamic modelling of wind turbine gearbox bearing loading during transient events. IET Renew Power Gener 2015;9:821–30. https://doi.org/10.1049/iet-rpg.2014.0194.
[28] Howard T. Development of a novel bearing concept for improved wind turbine gearbox reliability. University of Sheffield; 2015.
[29] Fischer K, Besnard F, Member S, Bertling L, Member S. Reliability-centered maintenance for wind turbines based on statistical analysis and practical experience. IEEE Trans Energy Convers 2012;27:184–95. https://doi.org/10.1109/TEC.2011.2176129.
[30] Reid A, Martinez I, Marshall M, Minniti T, Kabra S, Kockelmann W, et al. Mapping of axial plastic zone for roller bearing overloads using neutron transmission imaging. Mater Des 2018;156:103–12. https://doi.org/10.1016/j.matdes.2018.06.042.
[31] Zaretsky EVA. Palmgren revisited: a basis for bearing life prediction. Soc Tribol Lubr Eng Annu Meet 1997:18–22. https://doi.org/10.1080/05698190500225011.
[32] Jacobson B. The Stribeck memorial lecture. Tribol Int 2003;36:781–9. https://doi.org/10.1016/S0301-679X(03)00094-X.
[33] Drakopoulos M, Connolley T, Reinhard C, Atwood R, Magdysyuk O, Vo N, et al. I12: the joint engineering, environment and processing (JEEP) beamline at Diamond light source. J Synchrotron Radiat 2015;22:828–38. https://doi.org/10.1107/S1600577515003513.
[34] Withers PJ, Webster PJ. Neutron and synchrotron X-ray strain scanning. Strain 2001;37:19–33. https://doi.org/10.1111/j.1475-1305.2001.tb01216.x.
[35] Korsunsky AM, Liu J, Golshan M, Dini D. Measurement of residual elastic strains in a titanium alloy using high energy synchrotron X-ray diffraction. Exp Mech 2006;46:519–29. https://doi.org/10.1007/s11340-006-8250-2.
[36] Wigger T, Lupton C, Alshammrei S, Tong J, Marrow TJ, Earp P, et al. In situ mapping of normal strains in the field of a growing fatigue crack in a steel weld using digital image correlation and energy dispersive synchrotron X-ray diffraction. Int J Fatigue 2018;115:11–9. https://doi.org/10.1016/j.ijfatigue.2018.05.016.
[37] Sato S, Wagatsuma K, Suzuki S, Kumagai M. Relationship between dislocations and residual stresses in cold-drawn pearlitic steel analyzed by energy-dispersive X-ray diffraction. Mater Char 2013;83:152–60. https://doi.org/10.1016/j.matchar.2013.06.017.
[38] Lopez-Crespo P, Mostafavi M, Steuwer A, Kelleher JF, Buslaps T, Withers PJ. Characterisation of overloads in fatigue by 2D strain mapping at the surface and in the bulk. Fatigue Fract Eng Mater Struct 2016;39:1040–8. https://doi.org/10.1111/ffe.12463.
[39] Baimpas N, Drakopoulos M, Connolley T, Song X, Pandazaras C, Korsunsky AM. A feasibility study of dynamic stress analysis inside a running internal combustion engine using synchrotron X-ray beams. J Synchrotron Radiat 2013;20:316–23. https://doi.org/10.1107/S0909049513000885.
[40] Mostafavi M, Collins DM, Peel MJ, Reinhard C, Barhli SM, Mills R, et al. Dynamic contact strain measurement by time-resolved stroboscopic energy dispersive synchrotron X-ray diffraction. Strain 2017;53:1–13. https://doi.org/10.1111/str.12221.
[41] SKF. Cylindrical roller bearings, single row: NU 1010 ECP. 2019 accessed http://www.skf.com/group/products/bearings-units-housings/roller-bearings/cylindrical-roller-bearings/single-row-cylindrical-roller-bearings/single-row/index.html?designation=NU 1010 ECP, Accessed date: 28 March 2019.
[42] Hammami M, Martins R, Fernandes C, Seabra J. Friction torque in rolling bearings lubricated with axle gear oils. Tribol Int 2018;119:419–35. https://doi.org/10.1016/j.triboint.2017.11.018.
[43] Simpson C. pyXe: XRD strain analysis (Version v0.9.1). 2019http://doi.org/10.5281/zenodo.3339591.
[44] Polinder H, Haan SWH De, Dubois MR, Han JG. Basic operation principles and electrical conversion systems of wind turbines. Eur Power Electron Drives 2015;15:43–50. https://doi.org/10.1080/09398368.2005.11463604.
[45] Sheng S. reportWind turbine gearbox condition monitoring round robin study – vibration analysis. National Renewable Energy Laboratory,Technical Report 2012.
[46] DSS. ABAQUS Analysis User's Manual 2014;6. 14-2.
[47] ASM International. Atlas of stress-strain curves. second ed. ASM International; 2002.
[48] Guo YB, Liu CR. Mechanical properties of hardened AISI 52100 steel in hard machining processes. J Manuf Sci Eng 2002;124:1–9.
[49] Harris TA, Kotzalas MN. Essential concepts of bearing technology: rolling bearing analysis. fifth ed. CRC Press; 2006.